

# ARTICLE

## High-bandwidth Close-Range Information Transport through Light Pipes

Joowon Lim<sup>1\*</sup>, Jannes Gladrow<sup>1\*</sup>, Douglas Kelly<sup>1</sup>, Greg O'Shea<sup>1</sup>, Govert Verkes<sup>1†</sup>,  
Ioan Stefanovici<sup>1</sup>, Sebastian Nowozin<sup>1†</sup>, and Benn Thomsen<sup>1</sup>

\* Contributed equally to this work

† Work done at Microsoft Research

<sup>1</sup> Microsoft Research, 21 Station Road, Cambridge CB1 2FB, United Kingdom.

Corresponding author: Jannes Gladrow, [jannes.gladrow@microsoft.com](mailto:jannes.gladrow@microsoft.com)

# Abstract

Image retrieval after propagation through multi-mode fibers is gaining attention due to their capacity to confine light and efficiently transport it over distances in a compact system. Here, we propose a generally applicable information-theoretic framework to transmit maximal-entropy (data) images and maximize the information transmission over sub-meter distances, a crucial capability that allows optical storage applications to scale and address different parts of storage media. To this end, we use millimeter-sized square optical waveguides to image a megapixel 8-bit spatial-light modulator. Data is thus represented as a 2D array of 8-bit values (symbols). Transmitting 100000s of symbols requires innovation beyond transmission matrix approaches. Deep neural networks have been recently utilized to retrieve images, but have been limited to small (thousands of symbols) and natural looking (low entropy) images. We maximize information transmission by combining a bandwidth-optimized homodyne detector with a differentiable hybrid neural-network consisting of a digital twin of the experiment setup and a U-Net. For the digital twin, we implement and compare a differentiable mode-based twin with a differentiable ray-based twin. Importantly, the latter can adapt to manufacturing-related setup imperfections during training which we show to be crucial. Our pipeline is trained end-to-end to recover digital input images while maximizing the achievable information page size based on a differentiable mutual-information estimator. We demonstrate retrieval of 66 kB at maximum with 1.7 bit per symbol on average with a range of 0.3 - 3.4 bit.

**Keywords:** Information transport, Differentiable ray tracing, Multi-mode fiber, Light pipe, Information theory, Deep Learning, Spatial Light Modulator.

## INTRODUCTION

Transmitting optical images over a distance and retrieving them is a fundamental operation in many optical applications ranging from imaging to communication system<sup>1,2</sup>. Such image transport is essential in applications such as holographic optical storage<sup>3,4</sup> which is seeing renewed interest due to the increasing capacity and access rate requirements of cloud storage. For any optical storage solution to be competitive, it is crucial to compactly guide data-encoded optical images to multiple target locations in a storage media to fully utilize its capacity. Multi-mode fibers (MMF) are ideal for this purpose and have recently been explored in both imaging<sup>5</sup>, digital communication<sup>6</sup>, and augmented as well as virtual reality devices<sup>7</sup> as an alternative to bulky optical lenses, due to their compactness and ability to confine and propagate light. In theory, adequately sized MMFs support a high signal transmission capacity. However, when transmitting images through MMF, the image gets heavily distorted as propagation speeds of modes differ causing signal from the distal facet to deviate increasingly from the input signal to the proximal facet with increasing propagation length. This limits direct utilization of MMF in imaging and communication applications. Recent progress has been made in undoing such distortion, generally following either a transmission-matrix approach<sup>8–13</sup> which relies on pre-measuring distortions, or statistical approaches, e.g., based on neural networks (DNNs<sup>14–16</sup>). The aim in this work is to investigate maximal throughput of digital information through waveguides for large-pixel images as a function of image pixel number and waveguide length, and uncover fundamental mechanisms of information loss. Using a network of light pipes, this would allow optical storage applications to scale and address different parts of storage media. To ensure that information transmission is not limited by the mode cut-off of the waveguide, we consider millimeter-sized square optical waveguides rather than typical 100-micron circular fibers (see Fig. 1A). We refer here to these waveguides as light pipes. The square cross-section was chosen to be congruent with the shape of spatial light modulator (SLM) pixels which we aim to image using the light-pipe in our setup (see Fig. 1A). The information is encoded in the phase of the SLM pixels.

Each image consists of symbols encoding digital data. We transmit 315000 symbols at maximum and capture them oversampled on megapixel cameras (see Fig. 1B). Building a transmission matrix to model the propagation of light becomes impractical due to the quadratic increase of matrix size in the symbol number. DNN-based approaches have shown promising results for restoring natural images especially in the context of endoscopic applications<sup>14–16</sup>. Such images are usually compressible due to their lower entropy. Trained DNN used for input reconstruction may in this case memorize output features based on their internal weights rather than the input. Consequently, the ability to restore natural-looking images does not quantify well the performance of transmission and recovery systems. By contrast, high-entropy data images require faithful recovery without anticipation of any image feature.

In previous works on imaging through MMF, detection was either intensity-only<sup>17</sup>, which is inherently lossy, or based on off-axis holography<sup>10,18</sup>. In off-axis holography, one needs to ensure that 0-order and  $\pm 1$ -order

signals to not overlap, which comes at the cost of limiting the spatial bandwidth product<sup>19</sup>. In this work, we introduce an adaptation of the homodyne detector described in<sup>20</sup> using a dual camera system instead of a switchable retarder to measure the full optical field at the distal facet without limiting spatial or temporal bandwidth.

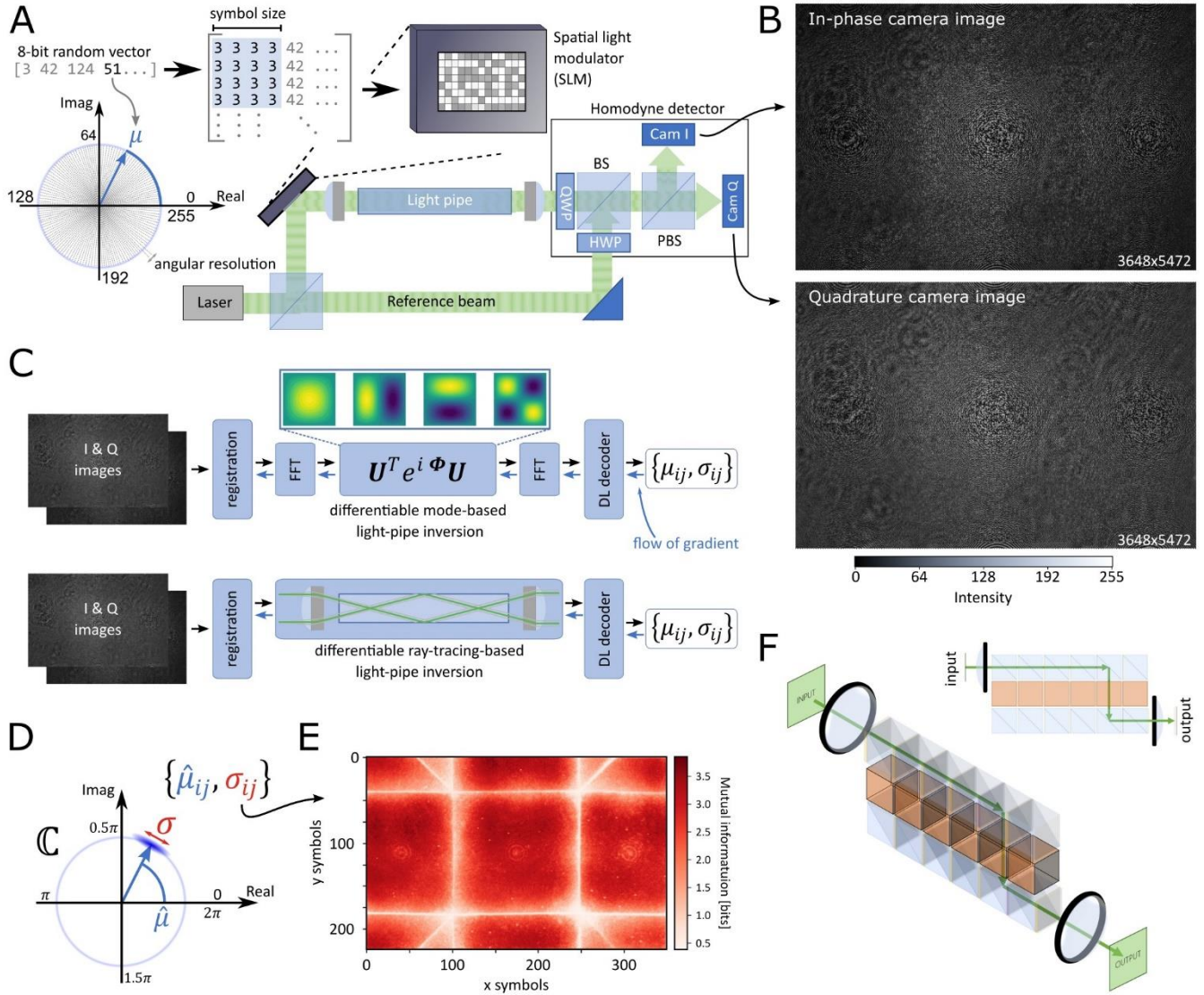


Figure 1. Main idea of the paper. **A** 8-bit symbols are displayed on a SLM over multiple pixels (decided by symbol size) to induce a phase delay of the signal beam. The signal beam modulated by the SLM is focused on the proximal facet, which is then followed by a light-pipe and another lens projecting to the homodyne detector. The sketch is not drawn to scale. QWP, HWP, BS, and PBS stand for quarter-wave plate, half-wave plate, beam splitter, and polarizing-beam splitter respectively. **B** Examples of in-phase and quadrature camera images captured using the homodyne detector. The images display severe phase distortion of the original data image. **C** Schematic description of decoding pipeline which consists of a localizer followed by a convolution-based decoder. The localizers can be either mode-based or ray-based. The localizers recover locality which is lost during light-pipe propagation. **D** The output of the decoder predicts the original phase value along with the uncertainty of the prediction. **E** Spatial total MI distribution retrieved from the uncertainty map for a symbol size of 4x4 pixels. **F** Sketch of the light-pipe data page routing concept. A sequence of cubic switches (light blue, e.g. polarization-based) form a light pipe and route data pages to and from the relevant locations inside an optical storage medium (orange).

Having access to the full electric field at the distal facet, we attempt to recover all information contained in the image. However, we show that on larger images (ex. over one million pixels for the 4x4 symbol size case) it is infeasible to invert the distortion process solely using a convolutional DNN due to a breakdown of locality, a property we define in this paper. To address this shortcoming, we introduce physics-based modules which pre-compensate for the distortion. The output of these specialized modules is then fed into a convolutional DNN. The overall decoder system is thus a hybrid of neural networks and physics-inspired pre-compensation modules (see Fig. 1C). We introduce two types of pre-compensation modules: First, we describe a mode-based approach using analytical descriptions of mode propagation for square-shaped light-pipes. However, the mode-based approach cannot handle deviations of the light-pipe from square cross sections (see supplementary), which we found to be unavoidable due to manufacturing tolerance. We therefore propose a second type of pre-compensation module, based on differentiable ray-tracing. This module is flexible enough to implement real-world light-pipe shapes and, crucially, enables us to adjust automatically to slight deviations of our light-pipe from a perfect square and even incorporate accurate models of the lenses we use in our setup. As a result, the ray-based model shows superior performance on experimental data than the mode-based approach. Both mode-based and ray-based localizers are differentiable which is critical as it allows us to jointly train further modules downstream from the pre-compensation modules. Specifically, our dual-camera detector requires image registration, which here too is learned, driven by gradients passed down through the specialized modules from the decoder.

Lastly, we describe a general framework to reason about the Shannon channel capacity of light-pipes and waveguides which relies on an estimation of the mutual information (MI) between SLM inputs and decoder outputs. MI is a measure between two random variables quantifying how much information is contained in one about the other. The estimated MI provides us with an upper bound to the number of bits that could possibly be transmitted. For each symbol location, the MI is estimated as a function of symbol size to study the ensuing trade-off between information per symbol and the number of symbols. A variational approach underpins our MI estimation<sup>21</sup>. The estimator is implemented as a convolutional Biternion neural-network<sup>22</sup> which is simultaneously trained to reconstruct the phase-shift imparted at the SLM and predict its uncertainty (see Fig. 1D). A spatially resolved MI map (see Fig. 1E) can then be calculated directly from the uncertainty without having to apply statistical estimators over hundreds of large images<sup>23</sup>. This is a general approach that should be applicable to other multi-mode channels. Moreover, our results are a first step towards demonstrating light pipes to be a viable, scalable, and manufacturable technology for routing data pages to target locations, albeit in distorted form, inside optical storage media as sketched in Fig. 1F.

## RESULTS

We propagate phase-encoded SLM images through a 2-f launch lens into a 75mm-long square-shaped light-pipe and, using another 2f-de-launch lens, onto a two-camera homodyne detector as shown in Fig. 1A. The homodyne detector simultaneously captures two images as in-phase and quadrature (see Fig. 1B) where

each camera detects the intensity of coherently summed signal and reference beams. The signal beam contribution to the quadrature image is a  $\pi/2$ -delayed version of that of the in-phase image such that both images combined give access to the full electric field. Please refer to the supplementary material for detailed explanation about in-phase and quadrature images.

In digital communication, binary messages are typically encoded in terms of symbols which can take values  $\{0, \dots, 2^b - 1\}$  where  $b$  is the bit-depth of the message. Each symbol is presented over a certain number of SLM pixels (see Fig. 1A). For a fixed SLM size, the total number of symbols therefore increases quadratically with decreasing symbol size. However, given the presence of noise in experiment, the smaller the symbol size (in pixels), the lower the signal-to-noise ratio, constraining the decodable bit-depth for each symbol. We utilized the full 8-bit depth of our SLM, that is, we set  $b = 8$  (see methods), to represent phased-coded data images, which are therefore 8-bit random matrices with a symbol size. Symbol sizes vary between 16x16 and 2x2 SLM pixels. The total amount of displayable information in a single image is thus  $N_y \times N_x \times 8$  bit ( $N_y$  and  $N_x$  represent the number of symbols not the number of pixels), and ranges from 4.8 kB to 2.5 MB as a function of symbol size. However, only a fraction of these theoretical data pages will be retrievable due to noise, quantization by cameras, and the scrambling induced by the light-pipe. Camera images are therefore processed by a light-weight decoder system consisting of a digital twin of the light-pipe and lenses as well as a convolutional neural network (CNN) (see methods) as shown in Fig. 1C. The role of the network is to retrieve the phase modulation at the SLM as a continuous angle and estimate the uncertainty of this prediction (see Fig. 1D). More precisely, our model is trained to predict parameters of a von-Mises distribution  $p(\vartheta|\mu, \kappa) = \frac{\exp(\kappa \cos(\vartheta - \mu))}{2\pi I_0(\kappa)}$  on the unit-circle where  $\vartheta$  is the true phase angle that we send to the SLM,  $\mu$  is the expected value of the phase angle, and  $\kappa$  denotes the concentration (inverse variance, i.e.  $\kappa_{i,j} = \sigma_{i,j}^{-2}$ ) of the distribution. For a pair of in-phase and quadrature input images, the network will thus output two matrices  $\mu_{ij}$  and  $\kappa_{ij}$ , i.e., mean and concentration values for each symbol (see Figs. 1C, 1D). Please see the supplementary for details of the implementation. Training is achieved by minimizing the negative log-likelihood of the true angle  $\vartheta$ . Predicting a full distribution of the phase angle rather than just the expected value enables us to make a spatially resolved MI estimate for each symbol. The MI (in bits) between symbol angles displayed on the SLM ( $\vartheta$ ) and angles predicted by the network ( $\mu$ ), can be written as

$$I_\kappa(\vartheta; \mu) = H(\vartheta) - H_\kappa(\vartheta|\mu) \approx \log_2(2\pi) + \int_0^{2\pi} p(\vartheta' | \mu, \kappa) \log_2(p(\vartheta' | \mu, \kappa)) d\vartheta' = -\log_2(I_0(\kappa)) + \kappa \frac{I_0(\kappa)}{\log(2) I_1(\kappa)}$$

where  $H$  denotes the entropies of the respective variables, while  $I_0$  and  $I_1$  denote the modified Bessel function of the first kind of order zero and one. The equation above assumes that all symbol angles are equally distributed which is approximately the case (see Fig. 1A). During training the MI increases driven by a decreasing network uncertainty. In Fig. 1E, we present one example of our results (4x4 symbol size) showing the estimated spatial distribution of MI.

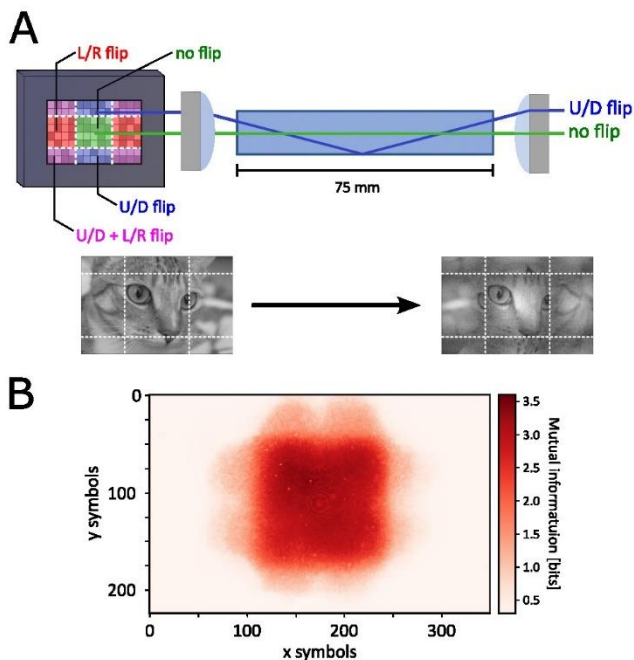


Figure 2. Delocalization of information and the receptive field of the CNN-based decoder without localizer. **A** Schematic description of delocalization within the light-pipe. Depending on the location on SLM, each pixel experience different numbers of total internal reflection. L/R means left/right, and U/D means up/down. The transformation is applied to Chelsea cat image as an example. The lens-induced global flip is corrected. **B** MI map obtained with a decoder without localizer.

In Fig. 2A, we explain how delocalization occurs within light-pipes using ray optics. Rays emanating from within the central zone of SLM propagate without any reflection. By contrast, rays coming from the up/down zones (blue ray) get reflected once. As a result, these zones appear flipped on the camera plane. The same happens along the horizontal direction. Therefore, without an inverting digital twin, the decoder is only able to estimate the symbol phase-profile at the central zone as shown in Fig. 2B. The light-pipe delocalizes parts of the input image over an area that exceeds the receptive field of the CNN (see methods and the supplementary). Algorithmically, the question of which symbol appears in which pixel is of quadratic order in the number of symbols (since we need to consider all possible combinations between symbols). In our case this is a prohibitively large number (315000 symbols at maximum). One typical approach to this problem is to measure and build a transmission matrix to map the electric field from the SLM plane to the camera plane<sup>8-11</sup>. To escape the quadratic scaling, we follow a similar approach, with the caveat that the transmission matrix does not appear explicitly but is inferred implicitly in our mode-based or ray-based digital twins. The main role of the digital twin is thus to restore locality to the image such that the network is given the information it needs to retrieve the phase profile on the SLM plane for each symbol. We hence refer to our digital twins also as localizers.



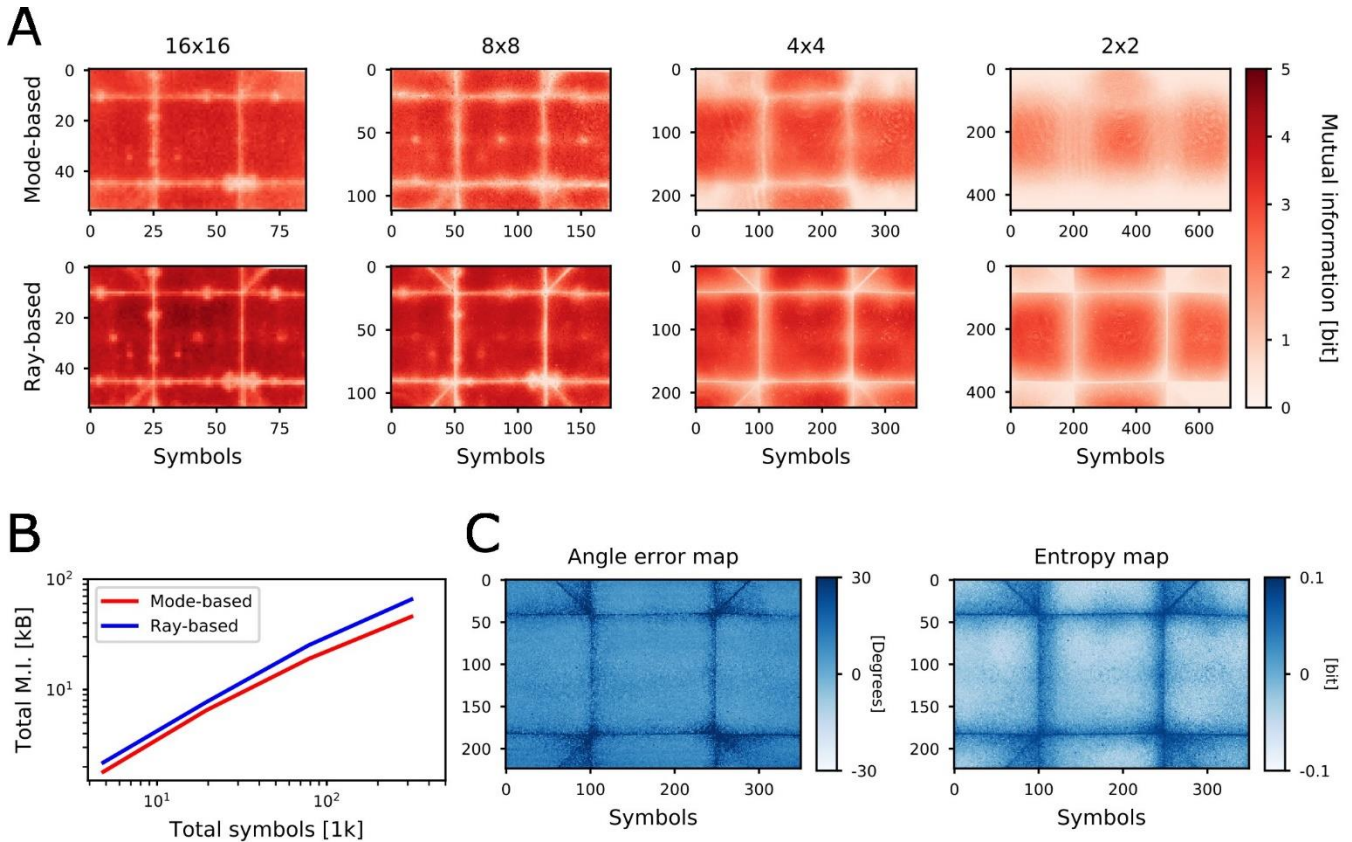


Figure 3. Total MI comparisons of experimental data with varying symbol size. **A** The first and second rows show the MI maps based on the mode-based and ray-based localizers, respectively. From left to right columns, the symbol size varies from 16x16 to 2x2 pixels. **B** Total MI for different symbol sizes shown in **A**. Total symbols denote the total number of symbols present in one image which increases with the decrease of symbol size. **C** A comparison between the estimated uncertainty from the decoder with the calculated differential entropy map from the test dataset.

By nature, the mode-based and ray-based localizers act in different ways: Our ray-based localizer only simulates the geometric aspects of our optical transmission pipeline. Therefore, the ray-based localizer outputs a grid of points on the camera indicating where rays emanating from symbols on the SLM impinge on the camera(s). This grid can then be used to reassemble the image in such a way that restores locality. For the ray-based localizer, inversion of the phase response is thus absorbed into the deep-learning decoder. Counter-intuitively, the ray-based pipeline is computationally light, since we can trace multiple rays in parallel and ray-tracing operations only need to be carried out during training. At test time, the grid is static and can simply be loaded. By contrast, the mode-based localizer, by virtue of being a wave-based model, is a richer representation of light-pipe propagation. It inverts the spatial delocalization as well as the modal phase dispersion and hence needs to be run at both test and training time. One would expect the mode-based-decoder pipeline to perform better than the ray-based approach given its physical accuracy. However, we show below that the opposite is the case for experimental data.



More precisely, we show that given the millimeter-scale of our light-pipe in our experimental measurements, the ray-based system is not only sufficient but superior to the mode-based localizer as shown in Fig. 3. In Fig. 3A, we vary the symbol sizes from 16x16 to 2x2 pixels, and display the total MI maps for both mode-based and ray-based localizers. A symbol size of 1x1 pixel results in 1.3M symbols leading to a low signal-to-noise ratio, too low for the camera registration module to converge. We therefore omit this datapoint here. In Fig. 3A, we show how much information can be encoded in different regions of SLM in terms of MI. The corresponding total MI values are plotted in Fig. 3B, confirming that the ray-based localizer outperforms the mode-based localizer in all cases. For instance, for symbol sizes of 4x4 and 2x2 SLM pixels, we obtain usable data page size of 19 kB and 46 kB using the mode-based localizer, and 25 kB and 66 kB using the ray-based localizer. This corresponds to retrieval ratios of 24.2% and 14.5% for symbol sizes 4x4 and 2x2 respectively. Finally, to confirm that our network faithfully predicts the uncertainty of its own phase prediction, we averaged the angle error over images in the test dataset and compared that to the averaged entropy map. A comparison in Fig. 3C shows consistency between the two images.

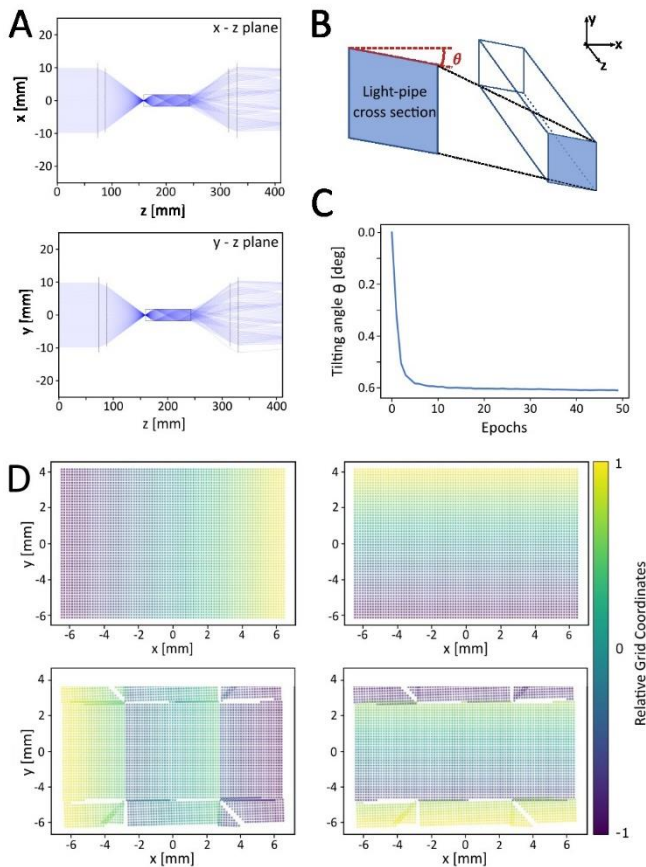


Figure 4 Differentiable ray tracing. **A** Plot of rays propagating through lenses and light-pipe. Each lens is a thick lens that consists of two materials (three surfaces). **B** Schematic description of the parallelogram angle. **C** The fitted parallelogram angle during training. **D** The top row display the positions of rays on the SLM plane and they are color-coded in  $x$  (left) and  $y$  (right) coordinate values, and the bottom row display the rays on the camera plane after propagating through a parallelogram light-pipe.

This is counterintuitive as the mode-based localizer is more accurate and able to capture the wave nature of light better than the ray-based localizer. However, unlike the mode-based localizer, the ray-based localizer is able to accommodate deviations of our experimental light-pipe from its designated shape and this results in better performance for realistic light-pipes. We discovered that the light-pipe deviates by a fraction of a degree from a perfect square shape and resembles a parallelogram, causing the modal shapes to differ from ones of a perfect square light-pipe (Please refer to the supplementary material for the derivation). In the first row of Fig. 3A, we can see the gradual degradation of total MI in the diagonal zones and, for small symbol sizes (4x4 and below), also in the top and bottom zones. We address this problem in the ray-tracing picture, where it is relatively straight-forward to relax the light-pipe shape into a parallelogram (see methods). Figure 4A shows ray propagation through our digital twin (a light-pipe along with two lenses). Moreover, since our ray-tracer is fully differentiable, i.e. is able to apply the chain rule to lens or light-pipe parameters, we are able to ‘fit’ the parallelogram angle during training of the full decoder system. The parallelogram angle converges to around  $-0.6^\circ$  (see Fig. 4B-C) starting from an initial value of  $0^\circ$ . This is an example of inverse ray tracing<sup>24–26</sup>: where we can (approximately) recover aspects of the geometry of our setup from acquired images without measuring them directly. In Fig. 4D, the top row displays the positions of rays on the SLM plane, color-coded in  $x$  and  $y$  coordinate values. The bottom row shows the ray positions on the camera plane after propagating through the parallelogram light-pipe. We can clearly see the overlap of rays in the diagonal zones, which explains why it is challenging to recover information in these diagonal zones particularly using the mode-based localizer. We use the ray-positions to resample camera images to restore locality. As a result, in Fig. 3A. we can see that the ray-based localizer can decode diagonal zones better than the mode-based localizer.

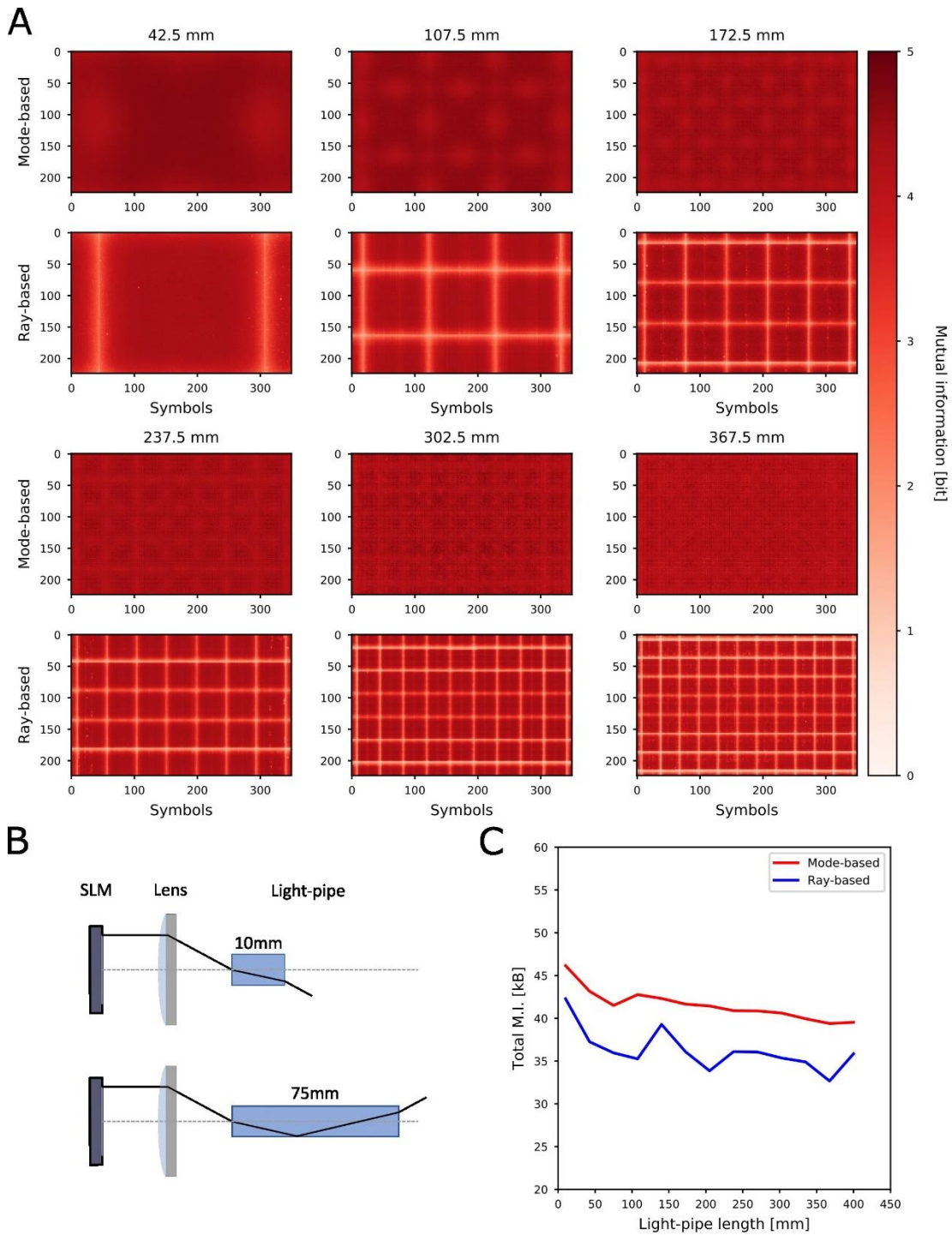


Figure 5. Results of simulation data for various light-pipe lengths. **A** Total MI maps for different light-pipe lengths using mode-based (the first and third rows) or ray-based (the second and fourth rows) localizers. **B** Schematic description of the increase in total internal reflection number with the increase of light-pipe length. **C** Quantitative evaluation of total MI per image with the length of light-pipe for two localizers.

To study the mechanism by which we lose information, we compare the performance of our localizers for different light-pipe lengths on synthetic data generated using simulations. While also being mode-based, the simulation is more accurate than the mode-based localizer. It includes a model of our homodyne detector system, lenses as well as a (perfect) square light-pipe (see methods). We vary the length of light-pipe from 10 mm to 400 mm at an interval of 32.5 mm. The 32.5-mm interval was chosen to increment the number of total internal reflections each time (In Fig. 5A, we show only subsets of them.). Due to the perfect square-shape in simulations, the mode-based localizer outperforms the ray-based localizer as we use approximately the same forward and inverse model for the light propagation as shown in Fig. 5B. Interestingly, in both cases, we observe the emergence of additional low MI regions (in-between squares) with increasing light-pipe length in Fig. 5A (compare to Fig. 3A). These are areas where locality jumps from one zone to another. In other words, local and non-local information on SLM is coherently summed, resulting in lowered intensity. In these areas several symbols overlap, making it harder for any decoder model to distinguish individual symbol values. The signal in these zones is thus more susceptible to noise resulting in lowered MI. Therefore, even for the mode-based localizer, we can see a decrease of total MI over increasing light-pipe length, a general mechanism of information loss. The ray-based localizer shares the same tendency, but it has a performance penalty compared to the mode-based localizer over increasing light-pipe length. In our ray-based model, we send only one ray per pixel, such that we cannot fully retrieve the electric field of symbols that spread over two or more locations. As a result, the ray-based localizer is more susceptible to the emergence of these regions. Since the camera sensor is rectangular, such regions appear along the horizontal direction first (Fig. 5A, 10mm). With increasing light-pipe length, there are discrete increments of these low MI regions which render the MI decrease non-monotonic. Nevertheless, in the previously discussed experimental case, the ray-based localizer outperforms the mode-based localizer as it can auto-adjust to the parallelogram-cross-section effectively.

## DISCUSSION

In this paper, we propose and demonstrate a framework for transmitting maximal-entropy images (data) through a light-pipe. Given that data is encoded in the phase of light, we utilize a homodyne detector to fully capture the phase information without limiting the spatial bandwidth. We can deliver up to 66 kB of information through the waveguide without relying on auxiliary imaging systems. However, the locality of original information is lost while light propagates through the light-pipe. If we solely rely on a convolutional DNN as decoder, we show that it can only decode the central region where the locality is preserved. Networks with all-to-all connectivity, such as transformer type networks<sup>27</sup>, are infeasible here due to their quadratic computational scaling with the number of inputs.

Therefore, we implement two localizers which exploit wave (mode-based) and ray (ray-based) properties of light. In theory, the mode-based localizer should be superior to the ray-based localizer. The ray-based model is generally flexible while the mode-based model requires analytical descriptions of eigenmodes of specific

geometric shapes such as square or cylinder. We implemented our ray-model to be differentiable so any gradient propagated from the loss function to the output of ray-tracer can be propagated through the ray-tracer whose parameters can then adjust to the experimental configuration. Therefore, the parallelogram angle of the light pipe is trainable so that it can adapt during training. We show that, by recovering aspects of the experimental set-up, the ray-based localizer performs better than the mode-based localizer. This ability of the localization-pipeline to adapt to and uncover optical geometry is, we believe, widely applicable in waveguide image transmission. In the simulation study, in Fig. 5, we can see the limitations of the current ray-based model, resulting from its inability to reconstruct symbols that scatter to multiple locations on the camera.

Lastly, through the paper, we used a DNN to predict the parameters of von-Mises distribution, which can be used to calculate the spatially-resolved MI distributions. As MI is a measure between two random variables, quantifying how much information is contained in one about the other, it provides an upper bound to the number of bits that could possibly be transmitted. This framework is thus general and can be applied to any information transportation system beyond what has been demonstrated in this work. In accord with theory, the MI only upper bounds the retrievable data page size per symbol. To use our channel as a communication channel, we need to retrieve symbols, that is, exchange the angle regression in our model for a symbol classification. In summary, we believe that our work opens a new route for maximal-information transmission through light-pipes and multi-mode fibers, along with a mechanism to self-calibrate during training. Furthermore, the ray-based framework could also be used to design optical hardware in conjunction with deep neural networks.

## **MATERIALS AND METHODS**

### ***Experimental Setup***

532nm light from a single longitudinal mode source is expanded and split between “signal” and “reference” paths by a polarizing beam splitter (PBS), with the ratio of power between each path controllable by adjusting the angle of a half wave plate. The reference beam is directed to the reference port of the homodyne detector system via a half wave plate to realign the reference polarization with the signal arm. The signal beam is reflected by a 50:50 beam splitter onto a nematic Liquid crystal on silicon SLM (Meadowlark HSP1920-488-800) comprising a  $1920 \times 1152$  array of  $9.2 \mu\text{m}$  pixels capable of imposing  $2\pi$  phase delay at 532 nm with 8 bits of precision. The reflected, encoded beam is transmitted by the beam splitter and is focused onto the input facet of the light-pipe by a  $f=80$  mm doublet (AC508-080-A-ML, Thorlabs). The output of the light-pipe is collected by a second  $f=80$  mm doublet and enters the signal port of the homodyne detector. The signal is converted to circular polarization by a quarter wave plate with fast axis oriented at  $45^\circ$  to the signal polarization. This introduces the required 90 phase shift between the two orthogonal polarization components of the signal before combining with the reference in the 50:50 beam splitter. The half waveplate in the reference arm is used to adjust the power of the reference between the two orthogonal polarization states.

Finally the in phase and quadrature components are split to two output ports by a PBS. At each output port is a camera (FLIR BFS-U3-200S6M-C) comprising an imaging chip of  $5472 \times 3648$   $2.4 \mu\text{m}$  pixels. Please refer to the supplementary material for a detailed explanation of the principles of the homodyne detector system.

**Decoder system:**

Our entire decoder pipeline, including the mode-based and ray-based localisers, was implemented in Pytorch (1.6)<sup>28</sup>. In the following, we give a summary of each component of this system.

- **Mode-based localiser:**

The propagation of TE-modes in a square-shaped light-pipe is a classic problem. The propagator of the electrical field can be obtained from solving Helmholtz' Equation  $\Delta E(x, y, z) + \epsilon_r(x, y, z)k^2E(x, y, z) = 0$  where  $E(x, y, z)$  is the electrical field, and  $\epsilon_r(x, y, z)$  and  $k$  are the relative electric permittivity value (which is square of refractive index value) and free space wave-number respectively. The equation comes with boundary conditions; here we assume absorbing boundaries as an approximation, i.e.,  $E(x, y, z) = 0$  on the boundaries. Then, we can represent the modes with sinusoidal bases with different mode propagation speeds. For the details, please refer to the supplementary material.

- **Ray-based localiser:**

Differentiable ray tracing has recently attracted a lot of attention<sup>24-26</sup>. Here, we implement a differentiable source-to-camera ray-tracer. Fundamentally, many aspects of ray tracing are differentiable: For instance, when a ray gets reflected by a partially absorbing surface, the amplitude of the ray is reduced by a factor, a linear operation that allows gradients to be computed with respect to this material parameter. Likewise, the position variable of rays can carry gradients with respect to the geometry of the optical setup. In our case, the most important variable is the parallelogram angle of our light-pipe as discussed in the results section. For further details, please refer to the supplementary material.

**Decoder U-Net architecture in detail:**

Our system captures in-phase and quadrature camera images, from which we sample to generate input images to the decoder. When transmitting  $(N_x, N_y)$  symbols (not pixels), we display one symbol over multiple pixels (decided by symbol size) and the pixel size of camera is smaller than that of SLM. When we sample camera images to generate input images to the decoder pipeline, and the sampled image size is  $(N_{sampling}N_x, N_{sampling}N_y)$ , where  $N_{sampling}$  represents the oversampling rate. For experimental data, we use different  $N_{sampling}$  values depending on symbol size ( $N_{symbol}$ ):  $N_{sampling} = 4$  (for  $N_{symbol} = 2$  and  $N_{symbol} = 4$ ),  $N_{sampling} = 8$  (for  $N_{symbol} = 8$ ),  $N_{sampling} = 16$  (for  $N_{symbol} = 16$ ). For simulation data, we use  $N_{sampling} = 4$ . (for  $N_{symbol} = 4$ ). Please refer to the supplementary material about details.

The input to decoder consists of 4 channel images: two sampled camera images and two positional encoding images ( $x$  and  $y$  2D grid images). We use a U-Net type architecture that consists of down-sampling blocks

followed by up-sampling blocks and a few convolutional layers<sup>29</sup>. The detailed structure is summarized in the supplementary material. After the up-sampling blocks, the image size is the same as the size of the input, and we need to further down-sample to match the number of symbols. In other words, as explained in the earlier section, the image size after the up sampling block is  $(N_{sampling}N_x, N_{sampling}N_y)$ , therefore, it is followed by additional convolution layers which perform down sampling to  $(N_x, N_y)$ , and we control the strides of the convolution layers depending on  $N_{sampling}$ . The details can be found on the supplementary material.

### **Training:**

For training, we use pre-recorded datasets from our setup or our simulation. For each page, we save the ground truth symbol value (8-bit integer) and the ensuing image. We can vary the symbol size, which determines the total symbol number. The total page numbers are 500 for all dataset. Training, validation, and test datasets are split with the ratio of 0.9, 0.05, and 0.05. The other training parameters and procedures are described in the supplementary material

### **ACKNOWLEDGMENTS**

We want to thank Sarah Lewis for discussions and her ongoing interest in the project. We also wish to thank Thomas Karagiannis, Babak Rahmani, Erika Aranas, as well as Bruno Magalhaes for fruitful discussions. Finally, we are deeply indebted to Hannes Schulz and the Amulet team for helping us with setting up our cloud-based ML training and testing pipeline.

### **CONFLICT OF INTERESTS**

The authors declare that they have no conflict of interest.

### **CONTRIBUTIONS**

J.L. wrote the text, carried out most of the computations and simulations and contributed to the code base, J.G. guided the research, carried out experiments, contributed to the text, and authored the code base. D.K. built and aligned the optical setup and contributed to figures. G.OS. developed the software for addressing the hardware and experiment automation. G.V. and I.S. contributed to the information-theoretic metric, I.S. further contributed to designing the decoder model. B.T. had the initial idea and supervised the project.

### **REFERENCES**

1. Flusberg, B. A. *et al.* Fiber-optic fluorescence imaging. *Nat Methods* **2**, 941–950 (2005).
2. Richardson, D. J., Fini, J. M. & Nelson, L. E. Space-division multiplexing in optical fibres. *Nat Photonics* **7**, 354–362 (2013).



3. Coufal, H. J., Psaltis, D. & Sincerbox, G. T. *Holographic data storage*. vol. 8 (Springer, 2000).
4. Chatzieftheriou, A., Stefanovici, I., Narayanan, D., Thomsen, B. & Rowstron, A. Could cloud storage be disrupted in the next decade? in *12th USENIX Workshop on Hot Topics in Storage and File Systems (HotStorage 20)* (2020).
5. Yoon, S. *et al.* Deep optical imaging within complex scattering media. *Nature Reviews Physics* vol. 2 141–158 Preprint at <https://doi.org/10.1038/s42254-019-0143-2> (2020).
6. Zhang, Y. *et al.* Impulse Response Characterization of a Commercial Multimode Fiber Using Superconducting Nanowire Single-Photon Detectors. *Journal of Lightwave Technology* **40**, 5107–5117 (2022).
7. Kress, B. C. Optical architectures for augmented-, virtual-, and mixed-reality headsets. in (Society of Photo-Optical Instrumentation Engineers, 2020).
8. Čižmár, T. & Dholakia, K. Exploiting multimode waveguides for pure fibre-based imaging. *Nat Commun* **3**, 1–9 (2012).
9. Choi, Y. *et al.* Scanner-free and wide-field endoscopic imaging by using a single multimode optical fiber. *Phys Rev Lett* **109**, 203901 (2012).
10. Loterie, D. *et al.* Digital confocal microscopy through a multimode fiber. *Opt Express* **23**, 23845–23858 (2015).
11. Popoff, S. M. *et al.* Measuring the transmission matrix in optics: an approach to the study and control of light propagation in disordered media. *Phys Rev Lett* **104**, 100601 (2010).
12. Stellinga, D. *et al.* Time-of-flight 3D imaging through multimode optical fibers. *Science (1979)* **374**, 1395–1399 (2021).
13. Li, S., Horsley, S. A. R., Tyc, T., Čižmár, T. & Phillips, D. B. Memory effect assisted imaging through multimode optical fibres. *Nat Commun* **12**, (2021).
14. Borhani, N., Kakkava, E., Moser, C. & Psaltis, D. Learning to see through multimode fibers. *Optica* **5**, 960–966 (2018).
15. Rahmani, B., Loterie, D., Konstantinou, G., Psaltis, D. & Moser, C. Multimode optical fiber transmission with a deep learning network. *Light Sci Appl* **7**, (2018).
16. Zhu, C. *et al.* Image reconstruction through a multimode fiber with a simple neural network architecture. *Sci Rep* **11**, (2021).
17. Zhao, T., Ourselin, S., Vercauteren, T. & Xia, W. Seeing through multimode fibers with real-valued intensity transmission matrices. *Opt Express* **28**, 20978 (2020).
18. Papadopoulos, I. N., Farahi, S., Moser, C. & Psaltis, D. High-resolution, lensless endoscope based on digital scanning through a multimode optical fiber. *Biomed Opt Express* **4**, 260–270 (2013).

19. Baek, Y., Lee, K., Shin, S. & Park, Y. Kramers–Kronig holographic imaging for high-space-bandwidth product. *Optica* **6**, 45–51 (2019).
20. Urness, A. C., Wilson, W. L. & Ayres, M. R. Homodyne detection of holographic memory systems. in *Optical Data Storage 2014* vol. 9201 92010Y (SPIE, 2014).
21. Poole, B., Ozair, S., Oord, A. van den, Alemi, A. A. & Tucker, G. On Variational Bounds of Mutual Information. (2019).
22. Prokudin, S. *Deep Directional Statistics: Pose Estimation with Uncertainty Quantification*.
23. MacKay, D. J. C. *Information theory, inference and learning algorithms*. (Cambridge university press, 2003).
24. Li, T. M., Aittala, M., Durand, F. & Lehtinen, J. Differentiable Monte Carlo ray tracing through edge sampling. in *SIGGRAPH Asia 2018 Technical Papers, SIGGRAPH Asia 2018* (Association for Computing Machinery, Inc, 2018). doi:10.1145/3272127.3275109.
25. Nimier-David, M., Vicini, D., Zeltner, T. & Jakob, W. Mitsuba 2: A retargetable forward and inverse renderer. *ACM Trans Graph* **38**, (2019).
26. Sun, Q., Wang, C., Fu, Q., Dun, X. & Heidrich, W. End-to-end complex lens design with differentiate ray tracing. *ACM Trans Graph* **40**, (2021).
27. Dosovitskiy, A. *et al.* An image is worth 16x16 words: Transformers for image recognition at scale. *arXiv preprint arXiv:2010.11929* (2020).
28. Paszke, A. *et al.* Pytorch: An imperative style, high-performance deep learning library. *arXiv preprint arXiv:1912.01703* (2019).
29. Ronneberger, O., Fischer, P. & Brox, T. U-net: Convolutional networks for biomedical image segmentation. in *International Conference on Medical image computing and computer-assisted intervention* 234–241 (2015).

# Supplementary materials

## 1. Decoder architecture

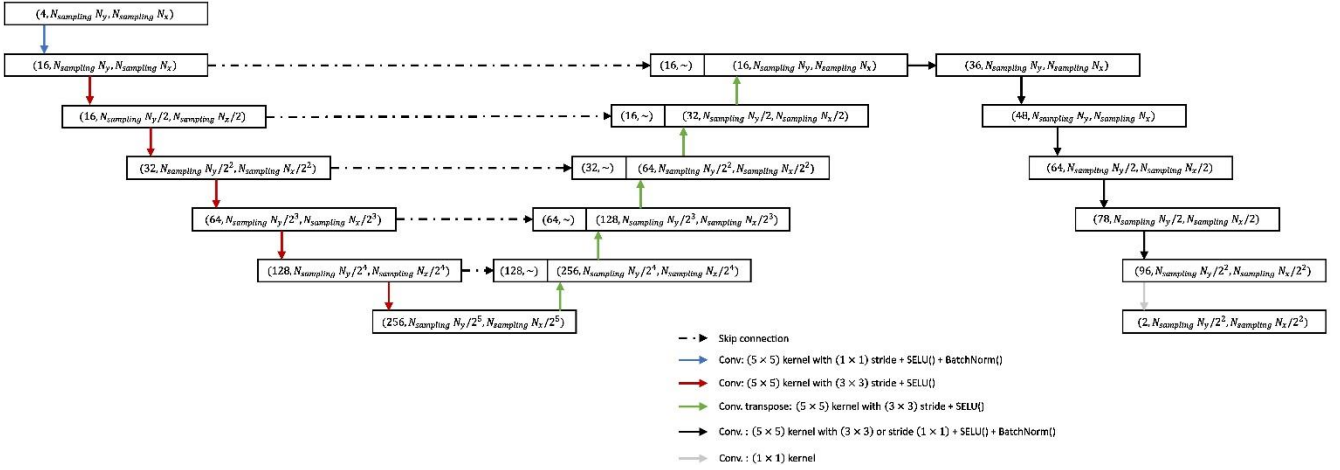


Figure S5. Schematic description of the decoder structure. In each block, the first number represents the channel number. The second and the third numbers represent the pixel numbers of image. For the skip-connection block, we only represent the channel number and omit the image pixels.  $N_{sampling}$  is a positive integer value to decide the sampling factor given symbol numbers along  $x$  and  $y$  axes,  $N_x$  and  $N_y$ , respectively.

The decoder network architecture is displayed in Fig. S1. The input has 4 channels: two sampled camera images and two positional encoding images ( $x$  and  $y$  2D grid images, shown in Figs. 4D and Fig. S4A, C). The input image size is  $(N_{sampling}N_x, N_{sampling}N_y)$  where  $N_{sampling}$  is a positive integer value to decide the sampling factor given symbol numbers along  $x$  and  $y$  axes,  $N_x$  and  $N_y$ , respectively. Depending on  $N_{sampling}$ , we adjust the stride values of convolution layers after the up-sampling blocks. In Fig. S1, the stride values for the convolution layers marked in black arrows are  $(1, 1, 3, 1, 3)$ , which result in a 4-times down sampling along each axis. The architecture in Fig. S1 is thus for  $N_{sampling} = 4$ . For  $N_{sampling} = 8$  and  $16$ , we change the stride values to  $(1, 1, 3, 3, 3)$  and  $(1, 3, 3, 3, 3)$ , respectively.

### 1. Parametrization of Network Outputs

As explained in the main text, our U-Net decoder predicts a phase-angle  $\mu_{i,j}$  and concentration  $\kappa_{i,j}$  for each symbol  $(i, j)$ . Letting the model directly output  $\mu_{i,j}$  and  $\kappa_{i,j}$  separately causes unwrapping problems at the  $0 - 2\pi$  boundary for  $\mu_{i,j}$ . It also requires neurons in the last layer to specialize to either angles or concentrations, leading to worsened performance and even numeric instability. We therefore let the model output a 2D vector  $\vec{p}_{i,j}$  for each symbol. The phase-angle is represented by the polar angle of  $\vec{p}_{i,j}$ ,  $\mu_{i,j} = \arctan2\left(\frac{p_{i,j}^y}{p_{i,j}^x}\right)$  while the norm of the vector controls the concentration, i.e.  $\kappa_{i,j} = \|\vec{p}_{i,j}\|$ .

### 2. Differentiable Bessel Functions

In order to implement the von-Mises-log-likelihood loss, we need a differentiable implementation of  $\log(I_m(\exp(x)))$  for  $m = 0, 1$  in pytorch. We use the following approximations <sup>1</sup>:

$$\log(I_0(e^x)) \approx \log(1 + 3.5156229 t(x)^2 + 3.0899424 t(x)^4 + 1.2067492 t(x)^6 + 0.2659732 t(x)^8 + 0.0360768 t(x)^{10} + 0.0045813 t(x)^{12}) \text{ for } x < \log(3.75) \text{ with } t(x) = e^x/3.75 \text{ and otherwise } \log(I_0(e^x)) \approx e^x - 0.5 x + \log(0.39894228 + 0.01328592 t(x)^{-1} + 0.00225319 t(x)^{-2} - 0.00157565 t(x)^{-3} + 0.00916281 t(x)^{-4} - 0.02057706 t(x)^{-5} + 0.02635537 t(x)^{-6} - 0.01647633 t(x)^{-7} + 0.00392377 t(x)^{-8}).$$

For  $m=1$ , we have for  $x < \log(3.75)$  ,  $\log(I_1(e^x)) \approx x + \log(0.5 + 0.87890594 t(x)^2 + 0.51498869 t(x)^4 + 0.15084934 t(x)^6 + 0.02658733 t(x)^8 + 0.00301532 t(x)^{10} + 0.00032411 t(x)^{12})$  and otherwise  $\log(I_1(e^x)) \approx e^x - 0.5 x + \log(0.39894228 - 0.03988024 t(x)^{-1} - 0.00362018 t(x)^{-2} + 0.00163801 t(x)^{-3} + 0.01787654 t(x)^{-7} - 0.00420059 t(x)^{-8}).$

### 3. Network training

In all cases, we use a batch size of 1, given the already high degree of weight-sharing over all symbols on a data page in our convolutional model. An additional, practical consideration here is the high memory load due to the large size of the input images. We use two different learning rates; one for the decoder parameters (see Table 1) and the other for the affine transform parameters (2e-4, please refer to Fig. S4 and the corresponding content regarding the affine transform). For both learning rates, we linearly warm up the learning rates to the target values (as noted in Table 1) for an epoch number corresponding to 2% of total epoch number. For the decoder learning rate, we damp it by the learning rate decay rate (see Table 1) at epoch numbers corresponding to 80% and 90% of total epoch numbers. In the case of the parallelogram-angle-fitting scenario (Fig. 4 in the main text), we use a different learning rate (1e-4 for experimental data and 0.0 for simulation data since the simulations are based on a perfect rectangular light-pipe) to update the parallelogram angle. We use the Adam optimizer<sup>2</sup> in all cases. When updating the decoder model parameters, we clip all gradients whose norm is larger than 1.0. For faster convergence, we initialize the diagonal values of the affine transform (scaling parameters). These values are set to approximately match the ratio between the field sizes of camera and spatial light modulator (SLM) in the  $x$  and  $y$  axes, respectively. These values are (0.98, 0.95). Also, for simulation data, when we use the ray-based localizer, we assume perfect paraxial lenses while we model actual compound lenses for experimental data.

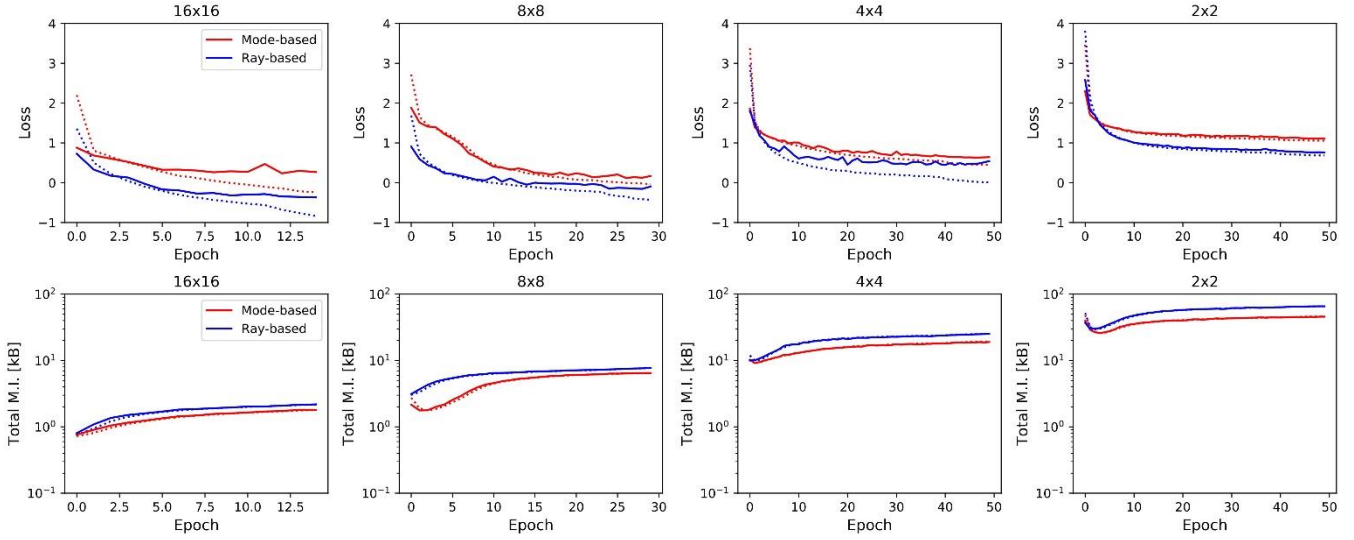


Figure S2. Train/validation loss (upper row) and total MI (lower row) curves for experiment data with various symbol sizes, and each symbol size is written on top of the graphs. The red and blue lines represent the mode-based and ray-based localizers, respectively. The dotted lines are train curves, and the solid lines are validation curves.

Figure S2 shows loss and total mutual information (MI) curves on train and valid datasets during training for different symbol sizes. As expected from the final performance shown in the main text, we can see that the ray-based localizer always higher MI values than the ones of the mode-based localizer. For smaller symbol sizes (8x8 and 16x16), we reduced the epoch numbers to 15 (16x16) and 30 (8x8), as they converge fast and start to be overfitted. Also, with the decrease of symbol size, the loss values become higher overall, which explain it becomes hard to extract information from smaller number of pixels.

Table 1. Training hyperparameters for experimental data.

	Symbol size	Epoch number	Decoder learning rate	Learning rate decay rate	Stride lists	$N_{sampling}$
Mode-based	2 x 2	50	1e-3	0.5	[1, 1, 3, 1, 3]	4
	4 x 4	50	1e-3	0.5	[1, 1, 3, 1, 3]	4
	8 x 8	30	1e-3	1.0	[1, 1, 3, 3, 3]	8
	16 x 16	15	1e-3	1.0	[1, 3, 3, 3, 3]	16
Ray-based	2 x 2	50	1e-3	0.5	[1, 1, 3, 1, 3]	4
	4 x 4	50	1e-3	0.5	[1, 1, 3, 1, 3]	4
	8 x 8	30	1e-3	1.0	[1, 1, 3, 3, 3]	8
	16 x 16	15	1e-3	1.0	[1, 3, 3, 3, 3]	16

Table 2. Training hyperparameters for simulation data.

	light-pipe length	Epoch number	Decoder learning rate	Learning rate decay rate	Stride lists	$N_{sampling}$
Mode-based	All cases	50	1e-3	0.5	[1, 1, 3, 1, 3]	4
Ray-based	All cases	50	1e-3	0.5	[1, 1, 3, 1, 3]	4

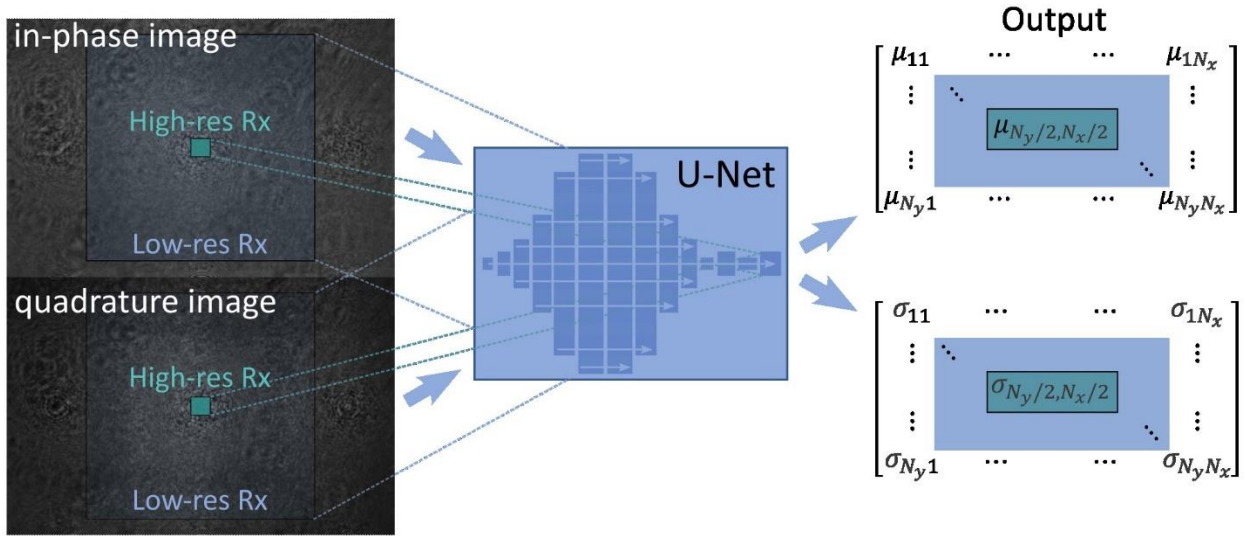


Figure S3. Receptive fields of the U-Net architecture. The U-Net processes the image on different spatial scales. The layers operating at the highest resolution are mainly responsible for decoding individual symbols but can consider information from the surrounding provided by coarser layers. The receptive field of the bottleneck ‘U’ part is denoted as ‘Low-res’ while the receptive field of the main branch of the network is denoted as ‘High-res’.

### 1. Receptive Field of our U-Net

As discussed in the main text and in Fig. S3, the need for special localizers arises because the convolution-based decoder, while efficient, has only a limited receptive field per symbol and a static set of convolutional kernels. In fact, the particular ‘U’ part of the U-Net structure endows the network with receptive fields on different resolutions: A top layer of the network ‘sees’ inputs on the highest resolution, while the down- and up-sampling layers (the ‘U-part’) of the network see the inputs on an exponentially coarser resolution, the deeper the layer. The deepest layers in the down-sampling part of the model can thus incorporate information on global illumination or global shifts of the grid. However, these layers cannot be expected to decode individual symbols, especially if the number of filters (channel number) is not high enough to route information from every symbol on the input side to every symbol to the output side. Combinatorially, the required filter number to achieve this may be prohibitively high and we never achieved this regime. In table 3, we list the receptive fields over the different branches of the U-Net.

Table 3 Receptive fields of different layers in the decoder. The down-and up-sampling layers are skipped here since they contribute information on a different coarseness as discussed in the text.

Layer	Kernel size	Stride	Receptive Field (size in symbols at $N_{sampling} = 4$ )
1	5	1	1.25
2	5	1	2.25

3	5	1	3.25
4	5	2	7.25
5	5	1	8.25
6	5	2	17.25
7	1	1	17.25

## 2. Detailed Description of Localizer Modules

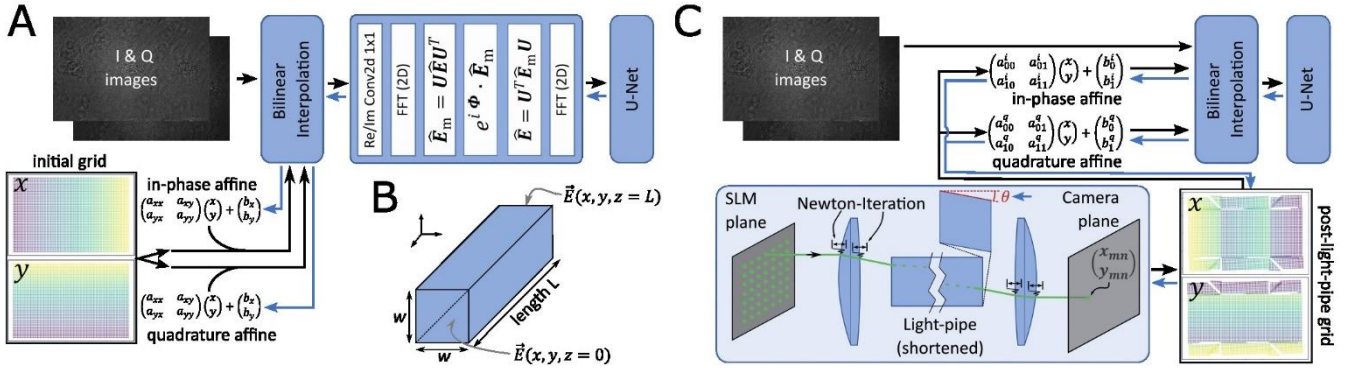


Figure S4: Details of the localizer modules. Forward operations are indicated by black arrows, while blue arrows indicate the flow of backward passes that build the gradient during training. **A** Mode-based localization pipeline as described in the text. **B** Description and definitions of variables of the light-pipe. **C** Ray-based localization pipeline. The localization in this pipeline is entirely handled by the sampling grid, which is obtained by ray-tracing through a precise digital twin of the setup. The light-pipe-parallelogram angle is shown in red to indicate that this variable receives a gradient and can be trained.

## 3. Mode-based localizer

The mode-based pipeline is shown in Fig. S4A. First, since our camera images are giga-pixel images, we down-sample the camera images to  $(N_{sampling}N_x, N_{sampling}N_y)$  where  $N_x$  and  $N_y$  represent symbol numbers (not pixel numbers) along  $x$  and  $y$  axes on SLM and  $N_{sampling}$  is the sampling rate we can control. To decide the sampling grid points on the camera images, we roughly estimate the start and end points along both  $x$  and  $y$  axes and perform equi-distance sampling, which give us  $x$  and  $y$  grid points. Since we use two cameras, the captured images from them should be well registered to each other in order to extract the electric field information. So, we apply affine transform independently on two independent sets of grids ( $x$  and  $y$  grids for I camera and another set of  $x$  and  $y$  grids for Q camera) to correct potential misalignment in real experiment. The sampled images are fed into the mode-based waveguide inversion, which again, is differentiable. The output of the mode-based inversion is then inserted into the U-Net decoder.

Here, we describe the inversion step in detail. The propagation of TE-modes in a square-shaped light-pipe is a classic problem. The propagator of the electrical field can be obtained from solving Helmholtz' Equation  $\Delta E(x, y, z) + \epsilon_r(x, y, z)k^2 E(x, y, z) = 0$  where  $E(x, y, z)$  is the electrical field, and  $\epsilon_r(x, y, z)$  and  $k$  are the relative electric permittivity value (which is square of refractive index value) and free space wave-number respectively. The equation comes with boundary conditions; here we assume absorbing boundaries as an



approximation, i.e.,  $\vec{E}(x, y, z) = 0$  on the boundaries. First, we describe the forward propagation through light-pipe. Given a square light-pipe whose width (height) and length are  $w$  and  $L$ , respectively, we can solve for the transversal field at the distal facet of light-pipe,  $E_z(x, y, z = L) = \sum_{n=1}^{\infty} \sum_{m=1}^{\infty} E_0^{(m,n)} \sin \frac{m\pi}{w} x \sin \frac{n\pi}{w} y e^{ik_z^{(m,n)}L}$  with  $k_z^{(m,n)} = \sqrt{(n_{lp}k)^2 - \left(\frac{m\pi}{w}\right)^2 - \left(\frac{n\pi}{w}\right)^2}$  and  $E_0^{(m,n)}$  denoting the mode coefficients at the frontal facet of light-pipe and  $n_{lp}$  is the refractive index value of light-pipe. Each mode coefficient,  $E_0^{(m,n)}$ , can be calculated by projecting the electric field at the frontal facet,  $E_z(x, y, z = 0)$ , onto the corresponding sinusoidal mode base,  $\sin \frac{m\pi}{w} x \sin \frac{n\pi}{w} y$ . For a discretized field,  $E_z(x_i, y_j, z = 0)$  where  $i = 1..N_x$  and  $j = 1..N_y$ , this can be efficiently implemented using matrix multiplication. In other words,  $E_0^{(m,n)}$  is the  $(m, n)$  component of the resulting matrix of  $U_y^T E_z(x_i, y_j, z = 0) U_x$ , where  $U_x = \left[ \sin\left(\frac{0\bar{x}\pi}{w}\right), \sin\left(\frac{1\bar{x}\pi}{w}\right), \dots, \sin\left(\frac{N_x\bar{x}\pi}{w}\right) \right]$  and  $U_y = \left[ \sin\left(\frac{0\bar{y}\pi}{w}\right), \sin\left(\frac{1\bar{y}\pi}{w}\right), \dots, \sin\left(\frac{N_y\bar{y}\pi}{w}\right) \right]$  given  $\vec{x} = [x_0, x_1, \dots, x_{N_x-1}]^T$  and  $\vec{y} = [y_0, y_1, \dots, y_{N_y-1}]^T$ . The mode coefficient at the distal facet can be calculated by multiplying  $E_0^{(m,n)}$  with the corresponding modal dispersion factor,  $e^{ik_z^{(m,n)}L}$ , resulting in  $E_L^{(m,n)}$ . By denoting the mode coefficient matrix at the distal facet as  $E_L$  and these coefficients can be transformed back to the image domain by calculating  $E_z(x_i, y_j, z = L) = U_y E_L U_x^T$ . The inversion step can be easily deduced from the forward step; we just need to use the conjugated value for the modal dispersion term, and the other processes stay unchanged. These operations can be implemented in Pytorch<sup>3</sup>, including the 2f-launch and 2f-delaunch lenses, which are modeled by fast Fourier transform. Since these mode transformations are differentiable due to Pytorch's ability to compute derivatives automatically, we add a 1x1-conv2d layer in front of the mode-based localized which acts separately on in-phase and quadrature images. For this convolution layer, we initialize weight values to 1 and bias values to 0. This allows the model to automatically account for any global phase offset or any difference in image-wide magnitudes between in-phase and quadrature images acquired from two different cameras. Downstream from the camera registration (which we explain below) and aforementioned 1x1-conv2d layer, we combine in-phase and quadrature tensors into a complex-valued 2D array.

#### 4. Ray-based localizer

The ray-based pipeline is shown in Fig. S4C. An initial grid of points (one set of  $x$  and  $y$  grids) on the SLM plane is used as origin of rays in our ray-based localizer. The rays propagate through the digital twin of the setup and get refracted at the first lens surface. We model our lenses as thick lenses which requires analytical descriptions of the lens surface shapes. Lens profiles are usually expressed in terms of the sag which quantifies the respective distance of the surface from the frontal or back plane of the lens. We define the sag as a function of the transversal distance from the optical axis,  $r$ :  $\text{sag}(r) = \frac{\kappa r^2}{1 + \sqrt{1 - Ar^2}}$  where  $A = (1 + c)\kappa^2$  with  $\kappa, c$  denoting the curvature and the conic coefficient, respectively. The gradient of the sag with respect to a coordinate position  $(x, y, z)$  can then be analytically derived which is sufficient to implement a Newton iteration

for the ray-surface intersection<sup>4</sup>. For our virtual lens, we use the curvatures and refractive index provided by the vendor (see experimental method section) such that we have a close analogue of the lens used in the experimental setup. For refraction, we apply Snell's law to each ray. The light-pipe is implemented as a refractive cuboid with dimensions  $3.56 \times 3.56 \times 75 \text{ mm}^3$ . The refractive index is  $n_{lp} = 1.461$ . Rays are propagated from the lens onto the frontal facet of the light-pipe where they refract. Inside the light-pipe, rays are reflected off the walls if they obey the total internal refraction angle. On the distal facet of the light-pipe, rays refract back into air and propagate onto the next lens where they get imaged onto the camera plane. In the ray-tracer, we ignore the optical elements of the homodyne detector (see Fig. 1 in the main text) and propagate the rays onto a single camera since we only need to extract positions of rays. Two independent affine transformations (for I&Q) are used again to ensures co-registration of the two cameras. The final grids are then used to sample the images using bilinear interpolation. The resulting image has a restored locality such that we can feed it into the U-Net decoder.

### 5. Mode analysis for a parallelogram light-pipe

Here, we try to find an analytical mode formulation for a parallelogram light-pipe and demonstrate how it differs from the one of a square light-pipe. First, we start from the same governing equation, Helmholtz' Equation:  $\Delta \vec{E}(x, y, z) + \epsilon_r(x, y, z)k^2 \vec{E}(x, y, z) = 0$ , with the absorbing boundary condition ( $E_{0,z}(x, y) = 0$  when  $x = w$  or  $y = w$  where  $w$  is the width/height of light-pipe.). We can represent a mode with propagation speed,  $\beta$ , as follows:  $E(x, y, z) = E_{0,z}(x, y)e^{i\beta z}$  where  $E_{0,z}(x, y)$  represents the mode profile in the transverse  $(x, y)$  plane. Plugging this in Helmholtz' Equation, it results in  $\left(\frac{\partial^2}{\partial x^2} + \frac{\partial^2}{\partial y^2}\right)E_{0,z}(x, y) + k_c^2 E_{0,z}(x, y) = 0$ , where  $k_c^2 = \epsilon_r(x, y, z)k^2 - \beta^2$ . In deriving the mode bases for a square light-pipe, we represent the solution of mode as  $E_{0,z}(x, y) = X(x)Y(y)$ , which is the multiplication of two independent functions ( $X(x)$  and  $Y(y)$ ) along  $x$  and  $y$  axes. Therefore, Helmholtz' Equation can be simplified as follows:  $\frac{1}{X(x)}\frac{\partial^2}{\partial x^2}X(x) + \frac{1}{Y(y)}\frac{\partial^2}{\partial y^2}Y(y) + k_c^2 = 0$ . Using the absorbing boundary condition, we can get  $X(x) = \sin\left(\frac{m\pi}{w}x\right)$  and  $Y(y) = \sin\left(\frac{n\pi}{w}y\right)$  and the modes are represented as the multiplication of these functions for various integer numbers ( $m$  and  $n$ ). We will apply the same logic for a parallelogram light-pipe, but we will represent the solution in  $y'$  axis  $E_{0,z}(x, y) = X(x)Y'(y')$ , where  $y' = x\sin\theta + y\cos\theta$  given a parallelogram angle  $\theta$ . By plugging it into Helmholtz' Equation, it results in  $\frac{1}{X(x)}\frac{\partial^2}{\partial x^2}X(x) + \frac{1}{Y'(y')}\frac{\partial^2}{\partial y'^2}Y'(y') - \frac{4\sin\theta}{(1+\sin^2\theta)X(x)Y'(y')}\frac{\partial}{\partial x}X(x)\frac{\partial}{\partial y'}Y'(y') + k_c^2 = 0$ . In this case, we have the term which depends both on  $X(x)$  and  $Y'(y')$ , which disappear when the parallelogram angle becomes 0. In other words, for a parallelogram light-pipe, we are not able to analytically model the mode as the multiplication of sinusoidal functions along  $x$  and  $y'$ .

### 6. In-phase and quadrature image formation

The homodyne detector shown in Fig 1A is configured such that the two cameras, when the optical path is unfolded, are coincident along the optical axis (by convention,  $z$ ). Thus, the captured in phase and quadrature

images can be used to generate the spatially- ( $xy$ -)varying real and imaginary parts of the field respectively at the single notional detection plane. To demonstrate this, we set out a simplified explanation of the formation of images in the homodyne detector where, for brevity, each of the optical components described (waveplates, beam splitter, polarizing beam splitter, camera) is assumed to perform ideally. In Fig. S5, we present how the polarization states change while the beams travel.

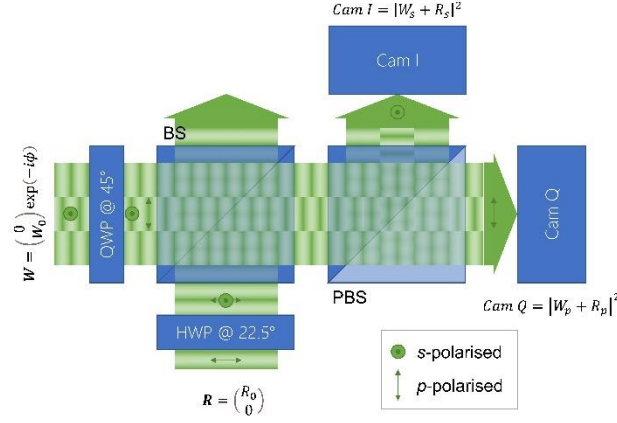


Figure S5 Illustration of the homodyne detector showing the polarization states at different positions in the system.

Consider the fields of the signal ( $W$ ) and reference ( $R$ ) beams before entering the homodyne detector. Omitting  $z$ -dependent phase for clarity, we can capture each field thus:

$$\begin{aligned} \mathbf{W} &= \begin{pmatrix} 0 \\ W_0 \end{pmatrix} \exp(-i\phi) \\ \mathbf{R} &= \begin{pmatrix} R_0 \\ 0 \end{pmatrix}, \end{aligned} \quad (1)$$

where the amplitude vector represents components in the ( $p$ ,  $s$ )-polarizations for each beam, and  $\phi = \phi_{SLM}(x, y)$  is the  $xy$ -varying phase retardation imparted on the signal beam by the SLM.

The actions of the quarter wave and half wave plates on the signal and reference beams respectively result in the beams at the entrance to the beam splitter being of the form:

$$\begin{aligned} \mathbf{W} &= \frac{1}{\sqrt{2}} W_0 \begin{pmatrix} \exp(i(-\phi + \pi/2)) \\ \exp(-i\phi) \end{pmatrix} \\ \mathbf{R} &= \frac{1}{\sqrt{2}} R_0 \begin{pmatrix} 1 \\ 1 \end{pmatrix}. \end{aligned} \quad (2)$$

In the implementation shown in Fig 1A, half of the light from each beam is discarded at the beam splitter; the other halves, now travelling coaxially, are routed according to polarization at the polarizing beam splitter such that the  $s$ -polarization of each beam is reflected, and the  $p$ -polarization transmitted. Then, the fields in each polarization can be written:

$$S = \frac{1}{2\sqrt{2}} [W_0 \exp(-i\phi) + R_0] \quad (3)$$

$$P = \frac{1}{2\sqrt{2}} [W_0 \exp(i(-\phi + \pi/2)) + R_0]$$

The cameras in the s- and p-polarization paths “see” the *intensity* of the field incident upon them:

$$|S|^2 = SS^* = \frac{1}{8} (W_0^2 + R_0^2 + 2W_0R_0 \cos \phi) \quad (4)$$

$$|P|^2 = PP^* = \frac{1}{8} (W_0^2 + R_0^2 + 2W_0R_0 \sin \phi).$$

Thus, following DC-subtraction and renormalization (processing, denoted by subscript *processed*) we can extract the in-phase ( $W_0 \cos \phi$ ) and quadrature ( $W_0 \sin \phi$ ) parts of the  $xy$ -varying field, and so infer the phase (and amplitude) encoded at the transmitter:

$$Field = I + iQ = |S|_{processed}^2 + i|P|_{processed}^2. \quad (5)$$

## References

1. Milton Abramowitz and Irene Stegun. *Handbook of Mathematical Functions with Formulas, Graphs, and Mathematical Tables*. (1972).
2. Kingma, D. P. & Ba, J. Adam: A method for stochastic optimization. *arXiv preprint arXiv:1412.6980* (2014).
3. Paszke, A. *et al.* Pytorch: An imperative style, high-performance deep learning library. *arXiv preprint arXiv:1912.01703* (2019).
4. Sun, Q., Wang, C., Qiang, F., Xiong, D. & Wolfgang, H. End-to-end complex lens design with differentiable ray tracing. *ACM Trans. Graph* **40**, 1–13 (2021).